J. Mech. Phys. Solids Vol. 39, No. 8, pp. 989–1015, 1991.
Printed in Great Britain.

0022–5096/91 \$3.00 + 0.00

FAMILY OF CRACK-TIP FIELDS CHARACTERIZED BY A TRIAXIALITY PARAMETER—I. STRUCTURE OF FIELDS

N. P. O'Dowd and C. F. Shih†

Division of Engineering, Brown University, Providence, RI 02912, U.S.A.

(*Received* 11 *June* 1990; *in revised form* 12 *November* 1990)

Abstract

Central to the J-based fracture mechanics approach is the existence of a HRR near-tip field which dominates the actual field over size scales comparable to those over which the micro-separation processes are active. There is now general agreement that the applicability of the J-approach is limited to so-called high-constraint crack geometries. We review the J-annulus concept and then develop the idea of a J–Q annulus. Within the J–Q annulus, the full range of high- and low-triaxiality fields are shown to be members of a family of solutions parameterized by Q when distances are measured in terms of J/σ_0, where σ_0 is the yield stress. The stress distribution and the maximum stress depend on Q alone while J sets the size scale over which large stresses and strains develop. Full-field solutions show that the Q-family of fields exists near the crack tip of different crack geometries at large-scale yielding. The Q-family provides a framework for quantifying the evolution of constraint as plastic flow progresses from small-scale yielding to fully yielded conditions, and the limiting (steady-state) constraint when it exists. The Q value of a crack geometry can be used to rank its constraint, thus giving a precise meaning to the term crack-tip constraint, a term which is widely used in the fracture literature but has heretofore been unquantified. A two-parameter fracture mechanics approach for tensile mode crack tip states in which the fracture toughness and the resistance curve depend on Q, i.e. $J_C(Q)$ and $J_R(\Delta a, Q)$, is proposed.

1. Introduction

The J-integral (Rice, 1968) and the HRR crack-tip field (Hutchinson, 1968; Rice and Rosengren, 1968) provide the basis for nonlinear fracture mechanics. To the extent that the HRR-singular field (scaled by J) exists and dominates the actual field over size scales comparable to those over which the micro-separation processes are active, a criterion for the onset of growth can be phrased in terms of the attainment of a critical value of J. Existence of a J-annulus in deeply cracked bend geometries has been shown by full-field numerical calculations. In tension-dominated crack geometries, the size of the J-annulus depends on the extent of plastic yielding and strain hardening properties. For example, it is known that when moderate-size tensile crack geometries (overall specimen size less than 20 cm) are loaded to general yield, the J-annulus is smaller than microstructurally relevant length scales and the zone of finite strains. These issues of J-dominance are discussed by McMeeking and Parks

† Author to whom correspondence should be addressed.

(1979), SHIH and GERMAN (1981), NEEDLEMAN and TVERGAARD (1983), and SHIH (1985). An excellent account of the status of the J-based approach can be found in a review article by HUTCHINSON (1983).

The limitations of a one-parameter J-based fracture mechanics approach have prompted investigators to consider various alternatives. Nevertheless an approach which advantageously uses and builds upon what is already known about the J-approach appears to be lacking. Recently, some progress has been made on two-parameter characterization of crack-tip states. LI and WANG (1986) showed that the high and low triaxial stress fields that develop at large-scale yielding can be characterized by J and a second parameter k_2 which is the amplitude of the second term of the asymptotic series of the small-strain plastic crack-tip fields. The values of k_2 were determined by matching the two-term expansion with the full-field solutions of SHIH and GERMAN (1981) and NEEDLEMAN and TVERGAARD (1983). BETEGÓN and HANCOCK (1990) and AL-ANI and HANCOCK (1991) have successfully matched the different near-tip fields at large-scale yielding in bend and tension geometries with the small-scale yielding fields obtained by a modified boundary layer formulation based on the K_I-field and the T-stress of the asymptotic series of the elastic field. DRUGAN and CHEN (1989) and CHEN and DRUGAN (1990) have obtained an 'm-family' of fields for growing cracks in isotropic, incompressible, elastic–perfectly-plastic material which can reproduce the entire range of stress triaxiality that arises in mode I plane strain bending- and tension-dominant crack geometries.

In this study we build upon the above observations. We direct attention to the mode I plane strain stationary crack problem and adopt a geometrically rigorous formulation which takes full account of crack-tip blunting. We consider a two-term expansion of the plastic crack-tip fields in which Q is a dimensionless amplitude factor of the second-order field. The J–Q annulus is investigated using a two-parameter boundary layer formulation whereby the remote tractions are given by the K_I-field and the transverse T-stress. Each crack-tip field distribution is shown to be a member of a one-parameter family of solutions parameterized by Q when distances are normalized by J/σ_0. Specifically, the stress distribution and the maximum stress are determined by Q alone while J sets the size scale over which large stresses and strains develop.

Ordinarily a small-strain analysis would be adequate for the purpose of investigating the existence of a J–Q annulus. Nonetheless we undertook a finite deformation analysis because our objectives go beyond those of investigating the J–Q annulus. The finite geometry fields associated with blunting provide certain information not directly accessible from the small-strain analysis. For example, the blunted opening, given roughly by J/σ_0, sets the local size scale over which large stress triaxiality and large strain develop, and consequently the size scale on which microscopic ductile fracture processes may be presumed to act (RICE and JOHNSON, 1970; MCMEEKING, 1977).

Through detailed comparisons, we have shown that the Q-family of crack-tip fields continues to exist near the tip in different crack geometries at large-scale yielding when the relevant crack dimension L is much larger than J/σ_0. We show that Q is a measure of the stress triaxiality or constraint of the crack geometry. The Q-family of fields provides a framework for quantifying the evolution of constraint as plastic flow progresses from small-scale yielding to fully yielded conditions, and the limiting (steady-state) constraint when it exists.

2. J–Q ANNULUS

2.1. *Q-family of solutions*

Consider a boundary layer formulation in which the remote tractions are given by the first two terms of the small-displacement-gradient linear elastic solution (WILLIAMS, 1957),

$$\sigma_{ij} = \frac{K_I}{\sqrt{2\pi r}} f_{ij}(\theta) + T\delta_{1i}\delta_{1j}. \tag{2.1}$$

Using different combinations of the two loading parameters, K_I and T, near-tip plastic fields of different magnitudes are generated. Now observe that T has dimension of stress. Thus $(K_I/\sigma_0)^2$ or equivalently J/σ_0 provides the only length scale in the two-parameter boundary layer formulation. Therefore displacements and quantities with dimensions of length must scale with it. Furthermore, the fields can depend on distance only through $r/(J/\sigma_0)$, i.e. the fields are of the form

$$\sigma_{ij} = \sigma_0 f_{ij}\left(\frac{r}{J/\sigma_0}, \theta; T/\sigma_0\right). \tag{2.2}$$

Using numerical solutions generated by a small-strain analysis of the above boundary layer formulation BETEGÓN and HANCOCK (1990) have provided an approximate explicit relation for the hoop stress which is consistent with (2.2). However, their result is not suited for applications to fully yielded crack geometries since the T-stress has no relevance under fully yielded conditions.

It proves useful to identify members of the above family by a parameter Q which arises in the plasticity analysis. Looking ahead to applications to fully yielded crack geometries, we write

$$\sigma_{ij} = \sigma_0 f_{ij}\left(\frac{r}{J/\sigma_0}, \theta; Q\right), \quad \varepsilon_{ij} = \varepsilon_0 g_{ij}\left(\frac{r}{J/\sigma_0}, \theta; Q\right), \quad u_i = \frac{J}{\sigma_0} h_i\left(\frac{r}{J/\sigma_0}, \theta; Q\right), \tag{2.3}$$

where the additional dependence of f_{ij}, g_{ij}, and h_i on dimensionless combinations of material parameters is understood. Indeed our numerical solutions show that the stress and strain distributions with the same Q-value collapse onto a single curve when the distance from the tip is normalized by J/σ_0, i.e. the distributions depend on Q alone.

The crack-tip opening displacement δ_t, defined by the opening where the 45° lines drawn backwards from the crack tip intersect the deformed crack faces, has the form

$$\delta_t = d(\alpha\varepsilon_0, n, Q)\frac{J}{\sigma_0}. \tag{2.4}$$

Here the dimensionless factor d depends strongly on n but weakly on $\alpha\varepsilon_0$ and Q. This relation, which is a specialization of the last equation in (2.3), generalizes an earlier result derived from the HRR field alone (Shih, 1981). For an $n = 10$ material, $d \approx 0.5$.

The crack-tip fields in finite width crack geometries must also be of the form in (2.3) when the characteristic crack dimension L is much larger than J/σ_0. The argument requires that the material has sufficient strain hardening capacity so that the governing equations remain elliptic as the plastic deformation spreads across the ligament.

The form in (2.3) is also applicable to generalized plane strain and 3-D tensile mode crack-tip states. This can be argued by considering a neighborhood of the crack front which is sufficiently far away from its intersection with the external surface of the body. As $r \to 0$, the 3-D fields approach the 2-D fields given by (2.3) so that the Q-family of solutions still applies; however, the Q value will be affected by every nonvanishing T-term. Parks (1989) has discussed the three T-terms which arise in 3-D crack problems.

2.2. *Asymptotic series for power-law material*

In order to obtain more information about the nature of the fields in (2.3) we consider a two-term asymptotic expansion based on a small-strain theory. By taking advantage of the simplified form of the small-strain solution, a procedure for assigning a definite Q value to each member of the field in (2.3) is developed. The approach under discussion is completely general and can apply to both plane strain and plane stress formulations as well as mixed-mode fields. Our attention is directed to the mode I plane strain problem.

Consider a material which deforms under uniaxial tension according to

$$\varepsilon/\varepsilon_0 = \sigma/\sigma_0 + \alpha(\sigma/\sigma_0)^n, \tag{2.5}$$

where n is the strain hardening exponent, α a material constant, and ε_0 the reference strain given by σ_0/E, with E being the Young's modulus. Generalizing to multiaxial states by J_2 deformation plasticity theory leads to

$$\varepsilon_{ij} = \frac{1+\nu}{E} s_{ij} + \frac{1-2\nu}{3E} \sigma_{kk}\delta_{ij} + \frac{3}{2}\alpha\varepsilon_0\left(\frac{\sigma_e}{\sigma_0}\right)^{n-1}\frac{s_{ij}}{\sigma_0}. \tag{2.6}$$

Here s_{ij} is the deviatoric stress, $\sigma_e = \sqrt{3s_{ij}s_{ij}/2}$ is the effective stress, and ν is Poisson's ratio. Within a small-strain formulation, the mode I stresses can admit the following asymptotic expansion:

$$\frac{\sigma_{ij}}{\sigma_0} = \left(\frac{J}{\alpha\varepsilon_0\sigma_0 I_n r}\right)^{1/(n+1)} \tilde{\sigma}_{ij}(\theta; n) + Q\left(\frac{r}{J/\sigma_0}\right)^q \hat{\sigma}_{ij}(\theta; n) + \text{higher-order terms}, \tag{2.7}$$

where r and θ are polar coordinates centered at the tip [see Fig. 1(a)]. The first term in the above expansion is the HRR singularity (Hutchinson, 1968; Rice and Rosengren, 1968) with J as its amplitude. The second term has Q, a dimensionless parameter (undetermined by the asymptotic analysis), as its amplitude. The form of the second term is consistent with (2.3). The plane strain and plane stress angular

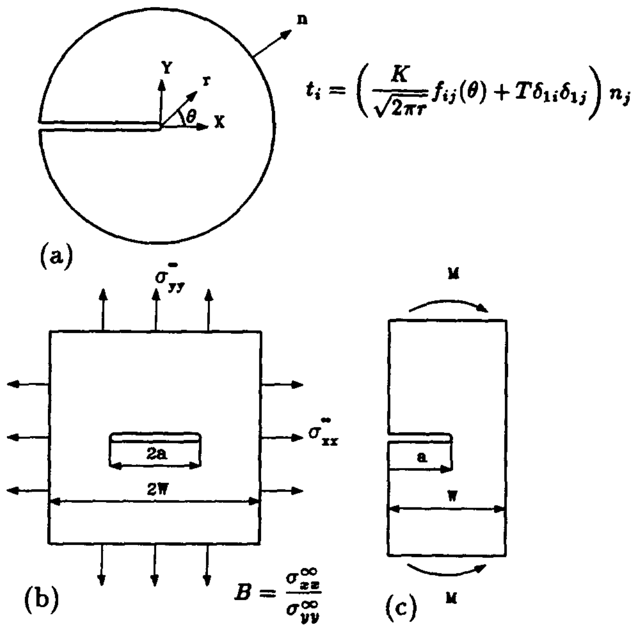

FIG. 1. Geometries investigated: (a) two-parameter boundary layer formulation, (b) biaxially loaded center-cracked panel, and (c) three-point bend bar.

functions $\tilde{\sigma}_{ij}$ and the integration constant I_n for $1 < n \leqslant 20$ have been tabulated by SYMINGTON *et al.* (1968).

2.3. *Fields in forward sector of the plastic zone*

For distances sufficiently close to the crack tip but still outside the zone of finite strains, the two-term expansion

$$\frac{1}{\sigma_0}\begin{pmatrix} \sigma_{rr} & \sigma_{r\theta} \\ \sigma_{r\theta} & \sigma_{\theta\theta} \end{pmatrix} = \left(\frac{J}{\alpha\varepsilon_0\sigma_0 I_n r}\right)^{1/(n+1)} \begin{pmatrix} \tilde{\sigma}_{rr} & \tilde{\sigma}_{r\theta} \\ \tilde{\sigma}_{r\theta} & \tilde{\sigma}_{\theta\theta} \end{pmatrix} + Q\left(\frac{r}{J/\sigma_0}\right)^q \begin{pmatrix} \hat{\sigma}_{rr} & \hat{\sigma}_{r\theta} \\ \hat{\sigma}_{r\theta} & \hat{\sigma}_{\theta\theta} \end{pmatrix} \qquad (2.8)$$

should adequately represent the actual in-plane stresses.

The method we have used to determine the essential features of the second-order term in (2.8) is described below. The full-field numerical solution to the two-parameter boundary layer formulation (2.1) is taken to be the exact solution. The second-order field is obtained by subtracting the HRR distribution (scaled by the applied J) from the full-field solution. An examination of the second-order field reveals that $|q| \ll 1$ and that the polar components of the second-order stresses $\hat{\sigma}_{ij}$ in the forward sector, $-\pi/2 \leqslant \theta \leqslant \pi/2$, vary slowly with θ. Moreover the magnitude of $\hat{\sigma}_{r\theta}$ is small compared to those of $\hat{\sigma}_{rr}$ and $\hat{\sigma}_{\theta\theta}$. Within the sector $|\theta| \leqslant \pi/4$, the ratio $\hat{\sigma}_{rr}/\hat{\sigma}_{\theta\theta}$ is nearly unity, i.e. the second-order field almost corresponds to a uniform hydrostatic stress state.

LI and WANG (1986) have investigated the second-order field using a numerical asymptotic expansion technique of the plane strain solution using the Airy stress function. Assuming that the second-order field has the same separable form for all values of θ, they have determined numerically that for $n = 3$, $q = -0.012$, and for $n = 10$, $q = 0.07$, i.e. the second-order terms are slowly varying functions of r. Their solutions have been confirmed by a recent numerical study of SHARMA and ARAVAS (1991) based on a Galerkin finite-element technique. For $5 \leqslant n \leqslant 20$, a range typical to ductile metals, the latter authors obtained q-values in the range $0 < q < 0.1$. The weak dependence of the second-order fields on r is consistent with our numerical results.

Our numerical results show that the full range of near-tip fields at large-scale yielding in different crack geometries are consistent with the Q-family of solutions constructed from the modified boundary layer formulation. Moreover we have found indirect support of our results in the analytical solutions of DRUGAN and CHEN (1989) and CHEN and DRUGAN (1990). They have obtained an 'm-family' of fields for growing cracks in isotropic, incompressible, elastic–perfectly-plastic material. While they did not provide results for the 'constant-stress' plastic sector ahead of the growing crack, they gave explicit forms for the second-order stress field in the extension of the 'centered-fan' plastic sector which extends from $45^\circ \leqslant \theta \leqslant 112^\circ$ for all m values. The field has this structure: $\hat{\sigma}_{r\theta} = 0$, $\hat{\sigma}_{rr}$ and $\hat{\sigma}_{\theta\theta}$ are independent of θ, and $\hat{\sigma}_{rr}/\hat{\sigma}_{\theta\theta} = 1/(1+m)$. As fully plastic conditions are approached, m assumes values ranging from 0 to about 2 for the geometries studied. These features of their growing-crack solutions are consistent with our numerically determined second-order solutions.

Based on our full-field solutions we suggest that the following two-term approximation of the expansion (2.8)

$$\frac{1}{\sigma_0}\begin{pmatrix}\sigma_{rr} & \sigma_{r\theta}\\ \sigma_{r\theta} & \sigma_{\theta\theta}\end{pmatrix} = \left(\frac{J}{\alpha\varepsilon_0\sigma_0 I_n r}\right)^{1/(n+1)}\begin{pmatrix}\tilde{\sigma}_{rr} & \tilde{\sigma}_{r\theta}\\ \tilde{\sigma}_{r\theta} & \tilde{\sigma}_{\theta\theta}\end{pmatrix} + Q\begin{pmatrix}\hat{\sigma}_{rr} & \hat{\sigma}_{r\theta}\\ \hat{\sigma}_{r\theta} & \hat{\sigma}_{\theta\theta}\end{pmatrix} \tag{2.9}$$

adequately represents the near-tip fields in the forward sector $|\theta| < \pi/2$. In the above representation, it is convenient to normalize the angular functions $\hat{\sigma}_{ij}(\theta)$ by requiring $\hat{\sigma}_{\theta\theta}(\theta = 0)$ equals unity. Since our calculations show that $\hat{\sigma}_{rr} \approx \hat{\sigma}_{\theta\theta}$ and $|\hat{\sigma}_{r\theta}| \ll |\hat{\sigma}_{\theta\theta}|$, Q is essentially a stress triaxiality parameter. We note that, if $\hat{\sigma}_{r\theta}$ vanishes, then the second-order term in (2.9) satisfies the equations of equilibrium to second order, if $\hat{\sigma}_{rr} = \hat{\sigma}_{\theta\theta} =$ constant [see also SHARMA and ARAVAS (1991)].

We do not dismiss the possibility that the second-order terms in (2.9), constructed in the manner described above, could include contributions from higher-order terms. The point to be made is this—the Q-family of solutions can be justified by the general result in (2.3) and the small-strain specialization (2.8). The latter is consistent with the solutions obtained by LI and WANG (1986) and SHARMA and ARAVAS (1991). We chose to work with the simpler approximate form in (2.9) for two reasons—to help with the interpretation of Q and to simplify the evaluation of Q in finite width crack geometries.

Using the two-term expansion (2.8) in (2.6) and retaining the two leading terms, the strains and displacements are of the form for $n > 2$

$$\frac{\varepsilon_{ij}}{\alpha\varepsilon_0} = \left(\frac{J}{\alpha\varepsilon_0\sigma_0 I_n r}\right)^{n/(n+1)}\tilde{\varepsilon}_{ij}(\theta) + Q\left(\frac{r}{J/\sigma_0}\right)^{q}\left(\frac{J}{\alpha\varepsilon_0\sigma_0 I_n r}\right)^{(n-1)/(n+1)}\hat{\varepsilon}_{ij}(\theta) \tag{2.10}$$

$$\frac{u_i - u_i^0}{\alpha\varepsilon_0} = \left(\frac{J}{\alpha\varepsilon_0\sigma_0 I_n}\right)^{n/(n+1)} r^{1/(n+1)}\tilde{u}_i(\theta) + Q\left(\frac{r}{J/\sigma_0}\right)\left(\frac{J}{\alpha\varepsilon_0\sigma_0 I_n}\right)^{(n-1)/(n+1)} r^{2/(n+1)}\hat{u}_i(\theta), \tag{2.11}$$

where u_i^0 are rigid body translations, and the dimensionless angular functions, $\hat{\varepsilon}_{ij}$ and $\tilde{u}_i$, for $1 < n \leqslant 20$ have been tabulated by SYMINGTON *et al.* (1988). The full-field strain and displacement solutions including the details of the dimensionless angular functions $\bar{\varepsilon}_{ij}$ and $\bar{u}_i$ will be discussed in Part II in connection with fracture mechanisms and criteria.

2.4. *Criteria for investigating the size of the* J–Q *annulus*

The plane strain Q-family of fields, (2.3), generated by the solutions to the two-parameter boundary layer formulation, provides the comparison fields for assessing the existence of the J–Q annulus. Our argument is as follows: if a J–Q annulus exists in a finite width crack geometry, then the stress and strain distribution near the tip, when the distance is normalized by J/σ_0, must match a member solution of the Q-family of fields.

An alternative and equally valid approach for investigating the existence of the J–Q annulus in a finite width crack geometry is by direct comparison of the near-tip fields with the small-strain two-term expansion in (2.8) or (2.9). Here it is necessary that the comparison be made over distances beyond the zone of finite strains. We have applied both criteria to the crack geometries under study, and in every case we reached similar conclusions regarding the size of the J–Q annulus.

3. NUMERICAL PROCEDURE

3.1. *Finite deformation plasticity*

The finite-element calculations use the semi-implicit integration method developed by MORAN *et al.* (1990). In this scheme, the deformation gradient is decomposed into elastic and plastic parts via

$$\mathbf{F} = \partial\mathbf{x}/\partial\mathbf{X} = \mathbf{F}^* \cdot \mathbf{F}^p, \tag{3.1}$$

where $\mathbf{x}$ is the current position of a material particle, and $\mathbf{X}$ is its position in the undeformed state. Here $\mathbf{F}^p$ is the deformation solely due to plastic flow, and $\mathbf{F}^*$ is the remaining contribution to $\mathbf{F}$. The stresses are computed from a hyperelastic potential, phrased in the so-called intermediate configuration obtained by applying the mapping $\mathbf{F}^p$ to the undeformed state. An isotropic neo-Hookean elastic response is assumed wherein

$$\mathbf{S}^* = \lambda \log (F^*)\mathbf{C}^{*-1} + \mu(\mathbf{I} - \mathbf{C}^{*-1}). \tag{3.2}$$

In (3.2) $\mathbf{S}^*$ is the second Piola–Kirchhoff stress on the intermediate configuration defined in terms of the Kirchhoff stress $\boldsymbol{\tau}$ as $\mathbf{S}^* = \mathbf{F}^{*-1} \cdot \boldsymbol{\tau} \cdot \mathbf{F}^{*-T}$, $F^* \equiv \det \mathbf{F}^*$, $\mathbf{C}^* = \mathbf{F}^{*T} \cdot \mathbf{F}^*$, $\mathbf{I}$ is the identity tensor, and λ and μ are the Lamé constants.

Plastic deformation is described by J_2 flow theory and the rate of plastic deformation $\mathbf{D}^{*p} = \text{sym}\,\{\dot{\mathbf{F}}^p \cdot \mathbf{F}^{p-1}\}$ phrased also on the intermediate configuration is given by

$$\mathbf{D}^{*p} = \dot{\bar{\varepsilon}}^p \,\text{sym}\,\{\mathbf{R}^*\}. \tag{3.3}$$

Here $\mathbf{R}^*$ is the current direction of the plastic deformation rate, and $\dot{\bar{\varepsilon}}^p$ is the effective plastic strain rate given by a flow law with strain hardening. In J_2 flow theory

$$\mathbf{R}^* = \frac{3}{2\bar{\sigma}}\,\mathbf{C}^* \cdot \mathbf{S}^{*\prime} \cdot \mathbf{C}^*, \tag{3.4}$$

where $\mathbf{S}^{*\prime}$ is the deviatoric part of $\mathbf{S}^*$ defined by $\mathbf{S}^{*\prime} = \mathbf{S}^* - 1/3(\mathbf{S}^* : \mathbf{C}^*)\mathbf{C}^{*-1}$. The effective stress, $\bar{\sigma}$, is defined as

$$\bar{\sigma}^2 = \tfrac{3}{2}(\mathbf{S}^{*\prime} \cdot \mathbf{C}^*) : (\mathbf{S}^{*\prime} \cdot \mathbf{C}^*). \tag{3.5}$$

In the present work, power law material strain rate sensitivity and strain hardening were assumed in the form

$$\begin{aligned} \dot{\bar{\varepsilon}}^p &= \dot{\varepsilon}_0 \left\{ \left[\frac{\bar{\sigma}}{H(\bar{\varepsilon}^p)} \right]^{1/m} - 1 \right\}, & \bar{\sigma} &\geqslant H(\bar{\varepsilon}^p) \\ \dot{\bar{\varepsilon}}^p &= 0, & \bar{\sigma} &\leqslant H(\bar{\varepsilon}^p) \end{aligned} \tag{3.6}$$

where

$$H(\bar{\varepsilon}^p) = \sigma_0 \left(1 + \frac{\bar{\varepsilon}^p}{\varepsilon_0} \right)^{1/n} \tag{3.7}$$

is a hardening function with exponent, n, σ_0 is a reference yield stress, ε_0 and $\dot{\varepsilon}_0$ are reference strain and strain rate, respectively, $\bar{\varepsilon}^p$ is the accumulated effective plastic strain, and m is the strain rate sensitivity exponent. To assess the effect of finite deformation the above formulation has been specialized to a small-strain version.

Our present study is restricted to rate-independent material behavior and test calculations with several crack problems show that rate-independent response is reproduced by using a value for m of 0.005. The rate of loading is such that the maximum strain rate is of the order of $\dot{\varepsilon}_0$ and no overstress is generated by rate dependence. Thus our analysis pertains to a rate-independent material of hardening exponent n and initial yield stress σ_0.

3.2. *Finite-element model*

The finite deformation analysis employs an assumed strain formulation which prevents locking associated with fully developed plastic flow. This is implemented using a four-node isoparametric element (Moran *et al.*, 1990).

For finite deformation analysis, the crack tip is assigned a finite root radius. In the boundary layer analysis, the initial notch radius is about 10^{-5} times the distance to the boundary at which tractions are applied. The ratio of the smallest to the largest element is also about 10^{-5} and the mesh in the radial direction is generated by exponential scaling. Because of symmetry we need only model the upper-half plane.

The mesh for the boundary layer analysis has about 1000 four-node elements. We experimented with several notch root radii and observed that once the crack tip has been blunted to about 3 times the initial notch root radius, the solutions did not depend on the initial root radius. A picture of a mesh similar to the one used here is given in MORAN *et al.* (1990).

A typical mesh for the finite width crack geometry has about 1200 elements. The results that we present are obtained with an initial notch root radius of about 10^{-5} times the characteristic crack dimension. Several different root radii were investigated, and as in the boundary layer calculations we found that the stress and strain distributions do not depend on the initial root radius when the crack tip has been blunted beyond about 3 times the initial root radius. Thus the solutions are independent of the initial root radius and may be interpreted as those pertaining to an initially sharp crack.

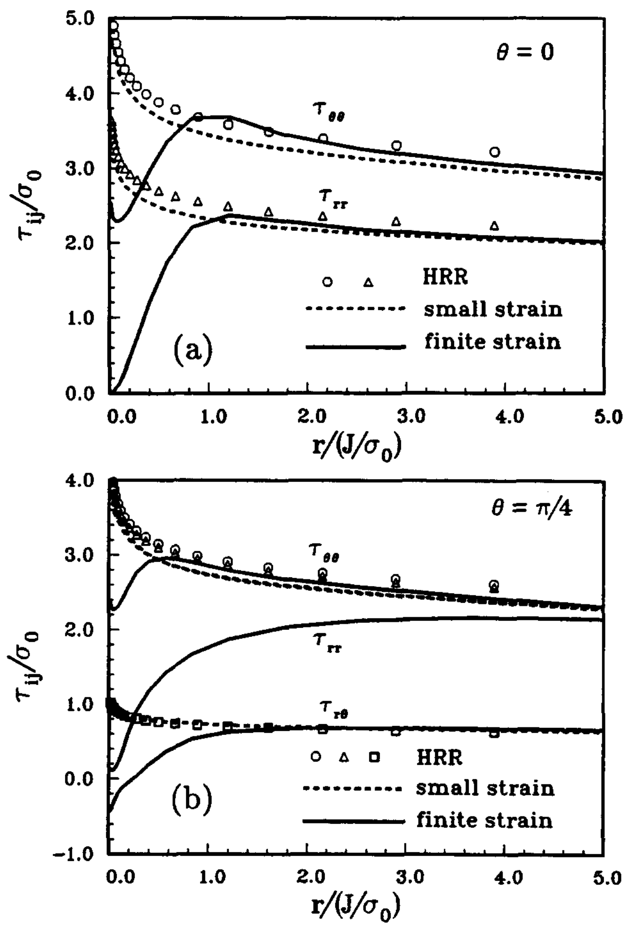

FIG. 2. Comparison of the small- and finite-strain solutions for $n = 10$ with the HRR field along: (a) $\theta = 0$, and (b) $\theta = \pi/4$.

4. Q-FAMILY OF FIELDS

Plane strain results are presented for a moderately hardening material characterized by $n = 10$, $\sigma_0/E = 1/300$, and reference strain ε_0, given by $\varepsilon_0 = \sigma_0/E$, where E is the Young's modulus. Poisson's ratio ν is taken as 0.3. To show that the overall features of the fields can be regarded as typical of materials with sufficient hardening capacity, selected results for $n = 5$ are also presented in Fig. 6.

4.1. *Two-parameter boundary layer formulation*

In the boundary layer formulation, the tractions consistent with the stresses in (2.1) are applied at the remote circular boundary of distance R, as shown in Fig. 1(a). LARSSON and CARLSSON (1973) demonstrated, by numerical solutions to the modified boundary layer problem, that the T-stress has a significant effect on the plastic zone size and shape, and that the small plastic zones in actual specimens are adequately predicted by the inclusion of the T-stress as a second crack-tip parameter. Their numerical results and the interpretation of T-stress effects given by RICE (1974) suggest that the near-tip stress distribution can be significantly affected by the T-stress though the value of the J-integral is unaffected. BILBY *et al.* (1986) have shown that negative T-stresses reduce the triaxial stress levels ahead of the crack. They also recognize that

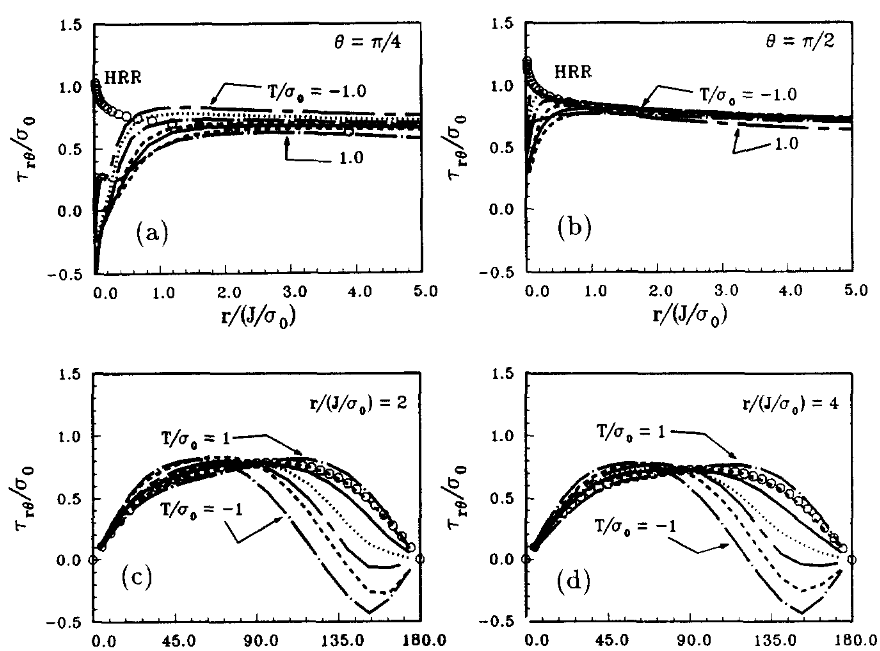

FIG. 3. (a) and (b) Radial distribution of shear stress for $-1 \leqslant T/\sigma_0 \leqslant 1$ at $\theta = \pi/4$ and $\pi/2$. (c) and (d) Angular distribution at $r/(J/\sigma_0) = 2$ and 4. The HRR field is indicated by the open circles.

the near-tip stress distribution depends on T, but is independent of K. Recently BETEGÓN and HANCOCK (1990), through the small-strain boundary layer formulation (2.1), provided details regarding the effect of T-stress on near-tip stress distribution, and have used these solutions to correlate the near-tip fields in several crack geometries at large-scale yielding.

Our calculations proceed by applying increments of K_I and T at the circular boundary of Fig. 1(a) while keeping the ratio T/K_I fixed throughout a particular analysis. We experimented with several different values of the ratio so that solutions at the desired value of T/σ_0 are obtained for different values of applied K_I. Small-scale yielding conditions are enforced by not allowing the plastic zone size r_p to exceed $0.2R$. We have confirmed that the stress distribution depends only on the value of T/σ_0 but is independent of K_I when distance is normalized by J/σ_0.

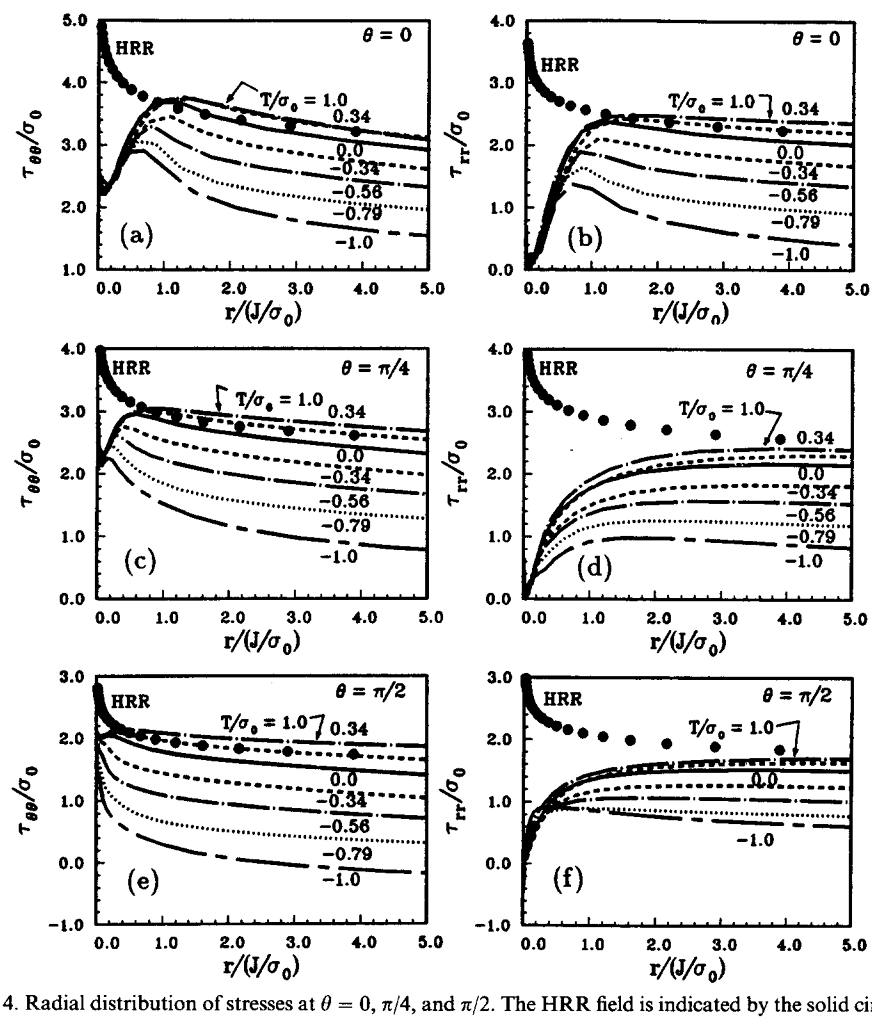

FIG. 4. Radial distribution of stresses at $\theta = 0$, $\pi/4$, and $\pi/2$. The HRR field is indicated by the solid circles.

The J-integral (RICE, 1968) in its finite deformation form (ESHELBY, 1970) is calculated by the domain integral method [e.g. LI *et al.* (1985), and MORAN and SHIH (1987)] which is a further development of the virtual crack extension method (PARKS, 1977). J shows a strong path dependence in the finite-strain zone and approaches zero for paths close to the blunted tip but is essentially path-independent for contours with mean radii greater than about $5\delta_t$. Beyond the zone of finite strains, the J value obtained agrees with the result $J = (1-\nu^2)K_I^2/E$ and does not depend on T.

Stress distributions obtained from the small- and finite-strain analysis for $T = 0$ are compared with the mode I HRR field in Fig. 2. Here r is the radial distance of the material in the undeformed state measured from the tip and is normalized by J/σ_0. θ is the angle measured from the crack line ahead of the tip. Stresses are normalized

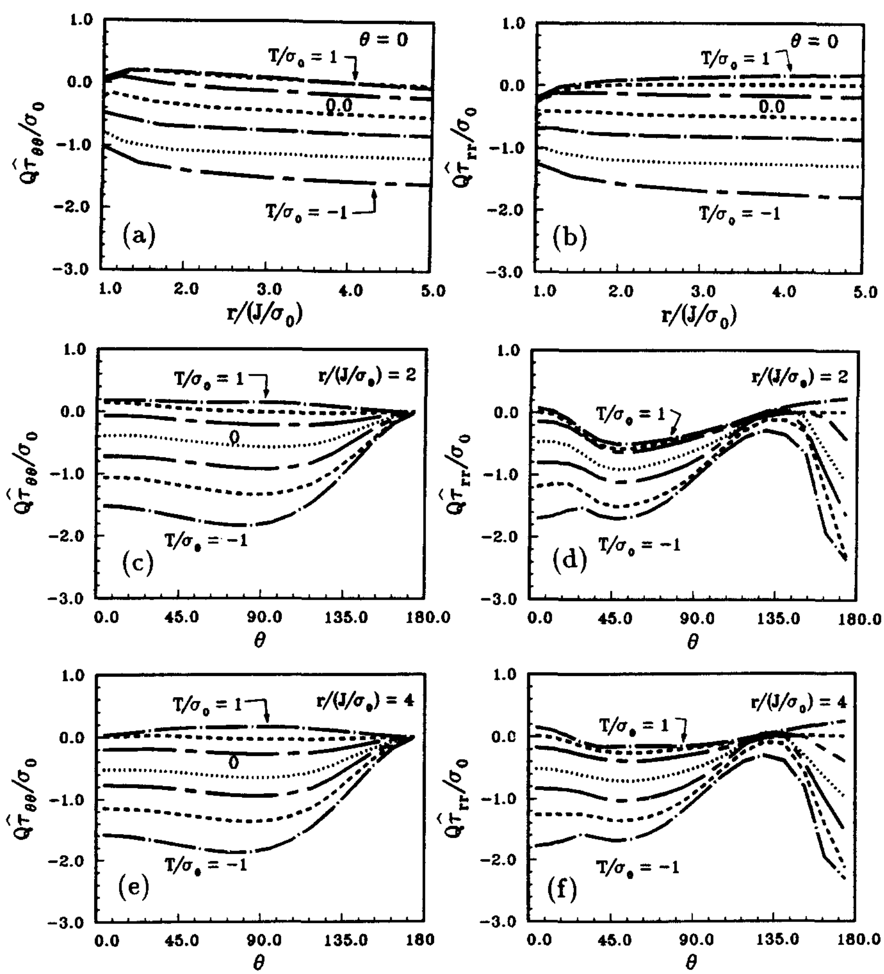

FIG. 5. Second-order stress terms. (a) and (b) Radial variation of normal stresses at $\theta = 0$. (c) and (d) Angular variation at $r/(J/\sigma_0) = 2$. (e) and (f) Angular variation at $r/(J/\sigma_0) = 4$.

by the yield stress σ_0. Within the distances shown, the small-strain solution indicated by the dash lines is within 6% of the HRR field indicated by the open symbols. Observe that the hoop and radial stresses of the HRR field are nearly identical at $\theta = 45°$. Likewise, the small-strain solutions for the hoop and radial stresses are almost indistinguishable at $\theta = 45°$.

For the finite-strain analysis we have plotted the Kirchhoff stress which is related to the Cauchy stress by $\boldsymbol{\tau} = \det(\mathbf{F})\boldsymbol{\sigma}$. For metals, $\det(\mathbf{F}) \approx 1$ so that $\boldsymbol{\tau} \approx \boldsymbol{\sigma}$. It can be seen that finite-strain effects are significant for $r/(J/\sigma_0) < 1$. In the interval $1 < r/(J/\sigma_0) < 3$, finite-strain effects are still evident. The hoop stress along $\theta = 0$ and $\pi/4$ is elevated slightly above the small-strain distribution and is actually closer to the HRR distribution. This behavior is in agreement with a well-known argument that

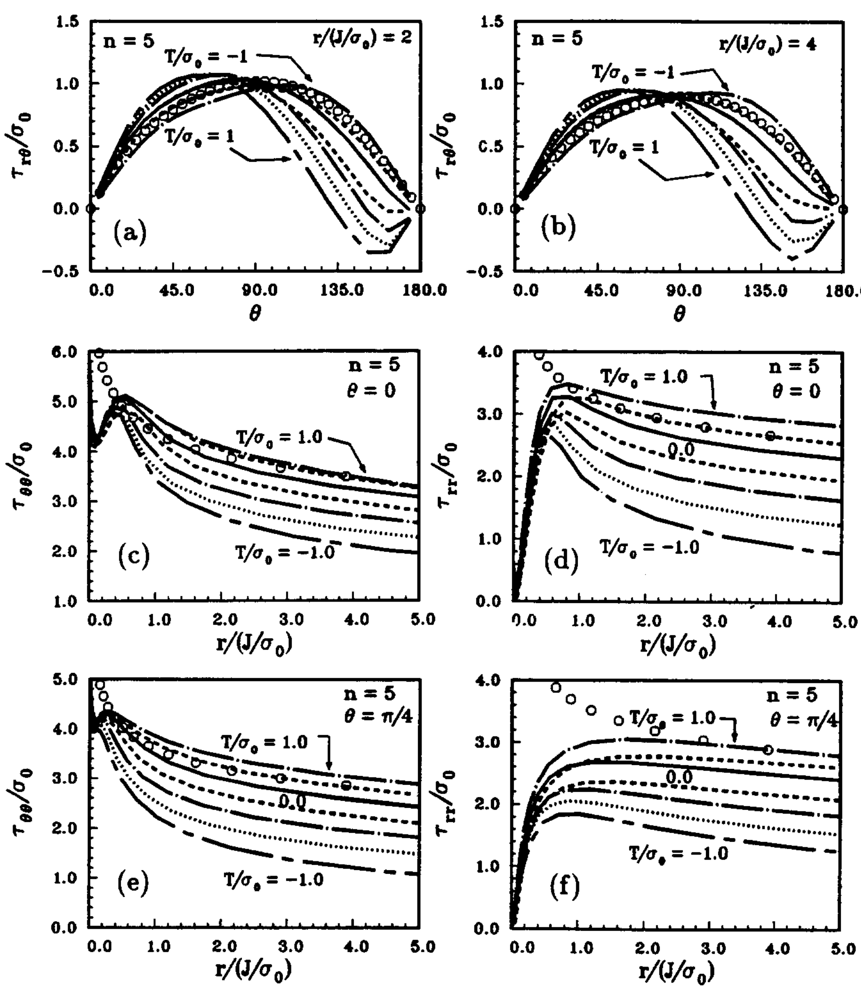

FIG. 6. Stress distributions for $n = 5$ material. (a) and (b) Angular distribution of shear stress at $r/(J/\sigma_0) = 2$ and 4. (c) and (d) Radial distribution of normal stresses at $\theta = 0$. (e) and (f) Radial distribution of normal stresses at $\theta = \pi/4$. HRR field indicated by open circles.

the tractions that would be supported by the region $r/(J/\sigma_0) < 1$ are transferred to the material ahead of the finite-strain zone, thus raising the hoop stresses in the interval $1 < r/(J/\sigma_0) < 3$.

The radial stress along $\theta = \pi/4$ shown in Fig. 2(b) is considerably lower than the small-strain solution and the HRR field. Beyond $r/(J/\sigma_0) = 3$ the small- and finite-strain stress distributions are in good agreement but are slightly below the HRR distribution. Surprisingly, there is good agreement between all three distributions for the shear stress at $\theta = \pi/4$ for $r/(J/\sigma_0) > 1$. This supports our observation that the second-order shear stress is vanishingly small.

The good agreement between the small- and finite-strain solutions allows us to use (2.9) to characterize the near-tip field.

4.2. *Construction of* Q-*fields*

T-stress in the range $-1 \leqslant T/\sigma_0 \leqslant 1$ is considered in the boundary layer analysis. Solutions for $|T/\sigma_0| > 1$ cannot be generated by the present boundary layer formulation since the condition that $R \gg r_p$ cannot be satisfied. Though not shown, a similar agreement between finite- and small-strain solutions to that seen in Fig. 2 has been observed for the range of T values considered. Thus we can apply the form of (2.9) to the finite-strain solutions to assign a Q value to every distribution obtained.

The angular and radial distributions of the Kirchhoff shear stress are shown in Fig. 3. The HRR field is indicated by the open circles. This comparison shows that the shear stresses in the sector $|\theta| < \pi/2$ for the full range of T/σ_0 are reasonably well predicted by the HRR distribution. The fields for $T/\sigma_0 = 0$, 0.34 and 1 continue to maintain agreement with the HRR field for $|\theta| > \pi/2$ whereas the agreement is poor for the fields for $T/\sigma_0 = -0.34$, -0.56, -0.79, and -1. Looking ahead to Figs 4 and 5 it can be seen that the second-order shear stress term within the forward sector is small in comparison with the other second-order stress components. By symmetry shear stress terms of all orders vanish at $\theta = 0$.

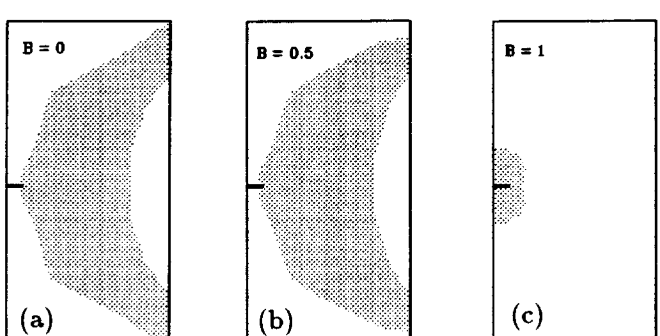

FIG. 7. Plastic zones in right half of center-cracked panel, $a/W = 0.1$, for $B = 0$, 0.5, and 1 at fully yielded conditions. Remote stress levels are $\sigma_{yy}^{\infty}/\sigma_0 = 1.1$, 1.9, and 2.0, respectively.

The radial variations of the hoop stress along $\theta = 0$, $\pi/4$, and $\pi/2$ are shown in Fig. 4(a), (c), and (e). It can be seen that the distribution for $T/\sigma_0 = 0$ agrees well with the HRR field (indicated by the solid circles) while the stress distributions for $T/\sigma_0 = 0.34$ and 1 lie slightly above the HRR distribution. The stress distributions associated with negative T-stresses fall considerably below the HRR distribution.

Using results obtained from a small-strain analysis Betegón and Hancock (1990) have provided a plot similar to Fig. 4(a). The trends of their solutions are similar to ours. However there are slight differences in the details. Du and Hancock (1991) have investigated T-stress effects in an elastic–perfectly-plastic material. Their numerical calculations for $T/\sigma_0 > 0.4$ produce stress distributions which approach the Prandtl field from below—the implication being that the HRR distribution is the limiting high-triaxiality distribution.

For $T/\sigma_0 > 0$, our calculations produce stress levels which are slightly higher than that for $T/\sigma_0 = 0$. Moreover the distributions for $T/\sigma_0 > 0.5$ appear to saturate at a level slightly above the HRR distribution. In light of the earlier discussion of finite-strain effects on the near-tip stresses, the limiting distribution may indeed be given by the HRR field.

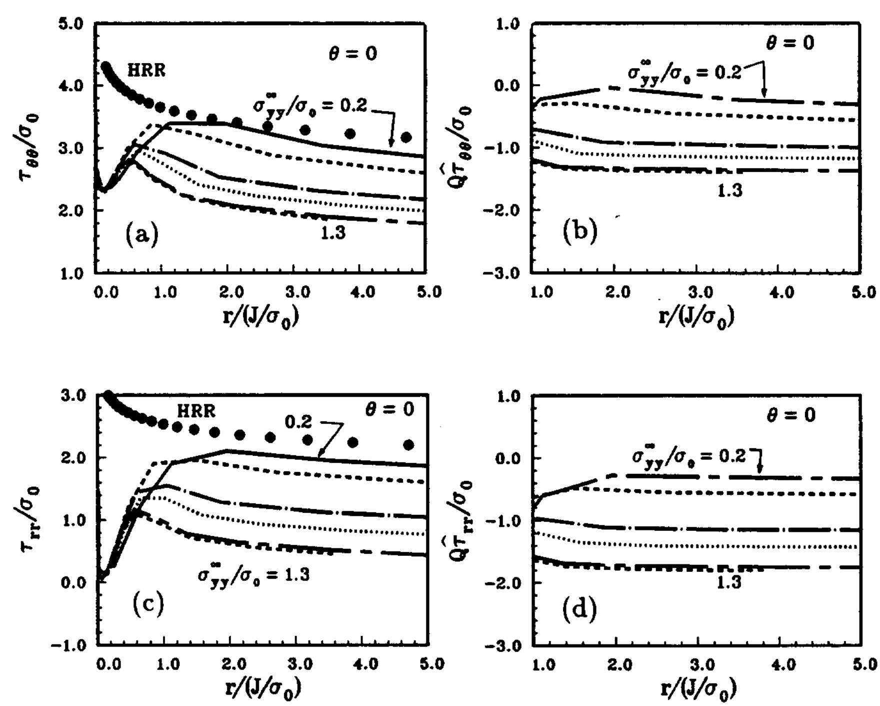

Fig. 8. Center-cracked panel, $a/W = 0.1$, and $B = 0$. Load levels are $\sigma^\infty_{yy}/\sigma_0 = 0.2$, 0.4, 0.8, 1.0, 1.25, and 1.3, corresponding to $a\sigma_0/J = 2640$, 650, 141, 70, 7, and 5. (a) and (c) Stress distributions at $\theta = 0$. HRR field is indicated by solid circles. (b) and (d) Second-order terms at $\theta = 0$.

The distribution of the radial stress at $\theta = 0$, $\pi/4$, and $\pi/2$ are shown in Fig. 4(b), (d), and (f). The stresses ahead of the crack for $T/\sigma_0 \geqslant 0$ agree well with the HRR distribution. Along $\theta = \pi/4$ and $\pi/2$ the radial stresses are slightly lower than the corresponding HRR stresses.

The second-order stress terms $Q\hat{\tau}_{\theta\theta}$ and $Q\hat{\tau}_{rr}$, defined as the difference between the full-field solution and the HRR field, are plotted in Fig. 5(a) and (b). Finite-strain effects dominate for $r/(J/\sigma_0) < 1$, while terms of higher order than Q can be significant at large distances. For these reasons, we show the fields in the interval $1 < r/(J/\sigma_0) < 5$. The weak dependence of $Q\hat{\tau}_{\theta\theta}$ and $Q\hat{\tau}_{rr}$ on distance r for $\theta = 0$ can be seen.

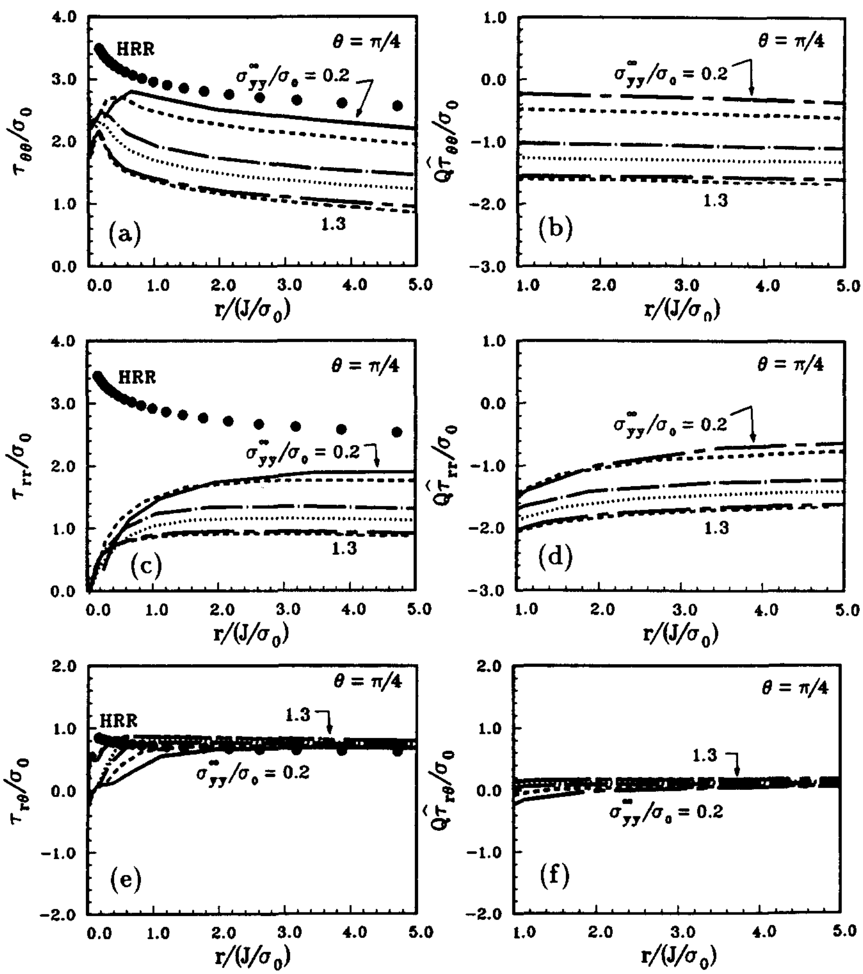

FIG. 9. Center-cracked panel, $a/W = 0.1$, and $B = 0$. Load levels as in Fig. 8. (a), (c) and (e) Stress distributions at $\theta = \pi/4$. HRR field is indicated by solid circles. (b), (d) and (f) Second-order terms at $\theta = \pi/4$.

Similar behavior is seen at all angles within the forward sector. Shown in Fig. 5(c)–(f) are the angular variations of $\hat{\tau}_{\theta\theta}$ and $\hat{\tau}_{rr}$ at two distances, $r/(J/\sigma_0) = 2$ and 4. The stresses vary slowly with θ in the sector $|\theta| < \pi/2$ and the ratio $\hat{\tau}_{\theta\theta}/\hat{\tau}_{rr}$ is close to unity here. Observe that the magnitudes of $Q\hat{\tau}_{\theta\theta}$ and $Q\hat{\tau}_{rr}$ are greater than that of $Q\hat{\tau}_{r\theta}$ as inferred from Fig. 3. All these features lend support to the form in (2.9) and allow us to interpret Q as the triaxiality parameter. Q values can be directly extracted from Fig. 5(a) since the angular functions $\hat{\tau}_{ij}$ are normalized by requiring $\hat{\tau}_{\theta\theta}(\theta = 0) = 1$.

It is natural to enquire if the above features are particular to an $n = 10$ material. To answer this question, we have plotted in Fig. 6 the solutions to the same boundary layer problem for $n = 5$ at the same values of T/σ_0. The features reported for the $n = 10$ material are also seen here.

The pattern of the plastic zones depends quite strongly on the T-stress. Tensile T-stresses cause the plastic zones to rotate backwards (towards the crack faces) and to shrink in size when lengths are normalized by $(K_I/\sigma_0)^2$. For large T-stresses, $T/\sigma_0 > 0.6$, the plastic zones rotate backwards and increase in size. Compressive T-stresses cause the plastic zones to expand in size along the direction of $\theta = \pm 60°$. The latter plastic zones are about 4 times larger than those induced by tensile T-stresses of comparable magnitude. Similar features were reported by LARSSON and CARLSSON (1973).

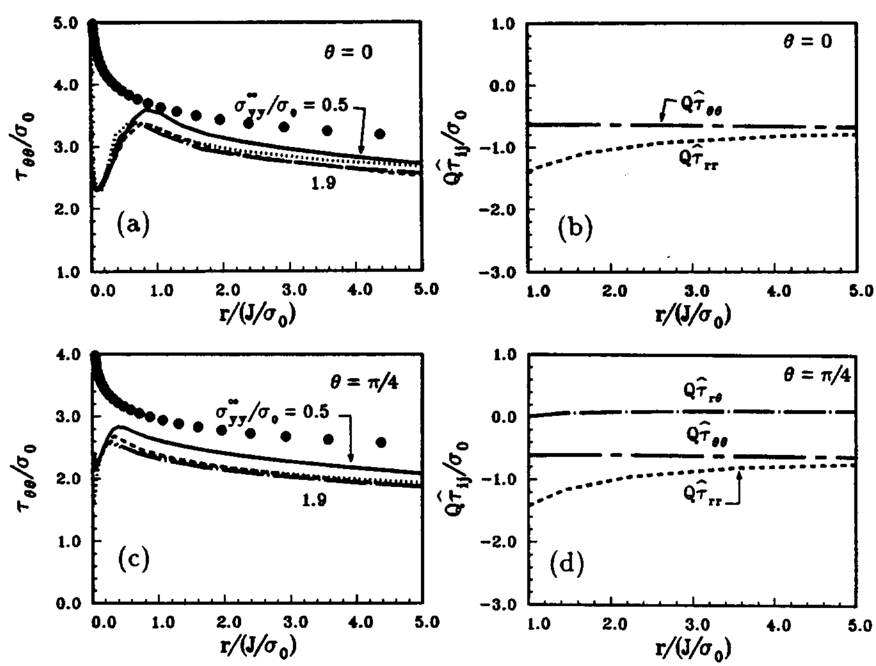

FIG. 10. Center-cracked panel, $a/W = 0.1$, and $B = 0.5$. (a) and (c) Hoop stress at $\theta = 0$ and $\pi/4$ for $\sigma_{yy}^{\infty}/\sigma_0 = 0.5$, 1.0, 1.5, and 1.9, corresponding to $a\sigma_0/J = 1400$, 85, 30, and 10. HRR field is indicated by solid circles. (b) and (d) Second-order terms at $\theta = 0$ and $\pi/4$ at the fully yielded state, $\sigma_{yy}^{\infty}/\sigma_0 = 1.9$.

5. Finite Width Crack Geometries

In this and subsequent sections we direct attention to finite width crack geometries. The material properties used in the calculations are the same as those described in Section 4. The plane strain results are discussed.

5.1. *Shallow crack tension geometry*, a/W = 0.1

The center-cracked panel loaded in biaxial tension is shown in Fig. 1(b). The state of biaxiality is given by $B \equiv \sigma_{xx}^{\infty}/\sigma_{yy}^{\infty}$. Three biaxiality ratios, $B = 0$, 0.5, and 1, are investigated.

Figure 7 shows the plastic zones in the right half of the panel at fully yielded conditions corresponding to $\sigma_{yy}^{\infty}/\sigma_0 = 1.1$, 1.9, and 2.0 for $B = 0$, 0.5, and 1, respectively. For biaxiality $B \geqslant 1$, the plastic zone does not spread across the ligament but instead it engulfs the crack completely. The stresses ahead of the crack for $B = 0$ are shown in Fig. 8(a) and (c). The corresponding HRR distributions scaled by the path-independent J value are indicated by the solid circles. At $\sigma_{yy}^{\infty}/\sigma_0 = 0.2$, corresponding to small-scale yielding, the full field is well approximated by the HRR field. As the load increases, the fields fall off substantially from the HRR distribution. These lower triaxiality stress distributions can be identified with members of the Q-family of fields

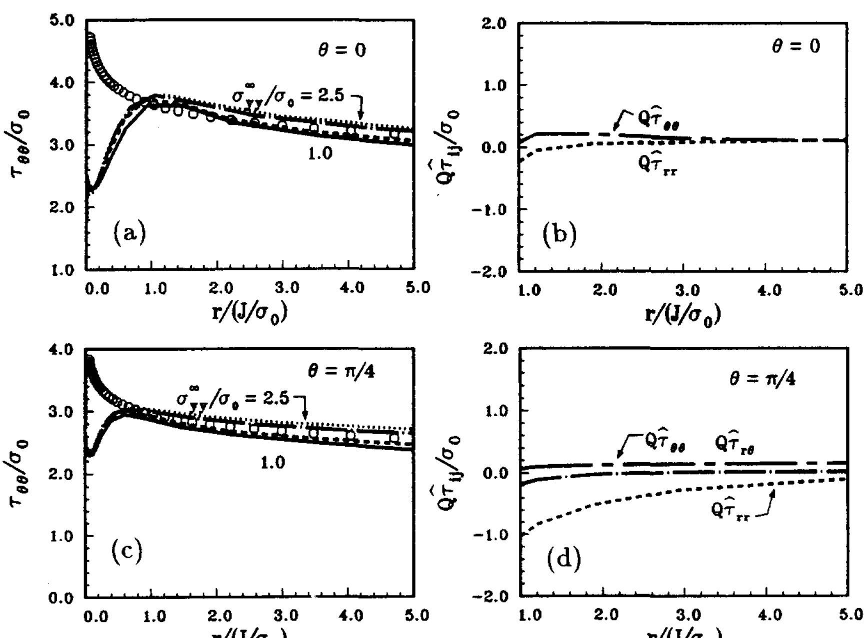

FIG. 11. Center-cracked panel, $a/W = 0.1$, and $B = 1.0$. (a) and (c) Hoop stress at $\theta = 0$ and $\pi/4$ for $\sigma_{yy}^{\infty}/\sigma_0 = 1.0$, 1.5, 2, and 2.5, corresponding to $a\sigma_0/J = 100$, 50, 20, and 10. HRR field is indicated by open circles. (b) and (d) Second-order terms at $\theta = 0$ and $\pi/4$ at the fully yielded state, $\sigma_{yy}^{\infty}/\sigma_0 = 2.0$.

discussed in Section 4. Figure 8(b) and (d) show the dependence of the second-order terms on the extent of yielding. Fully yielded conditions are reached at $\sigma_{yy}^{\infty}/\sigma_0 = 1.1$. Beyond this load level the stress distribution is unchanged and a steady-state Q value is obtained.

The distribution of the full field and the second-order terms along $\theta = \pi/4$ are shown in Fig. 9. Note that the behavior is similar to that for $\theta = 0$ and that the second-order shear stress term is essentially zero. Though the angular distributions are not shown, we have observed only weak angular dependence in the sector $|\theta| < \pi/2$.

Figure 10(a) and (c) show the stress distribution at $\theta = 0$ and $\pi/4$ for $B = 0.5$ at loads $\sigma_{yy}^{\infty} = 0.5$, 1.0, 1.5, and 1.9, corresponding to conditions which range from small-

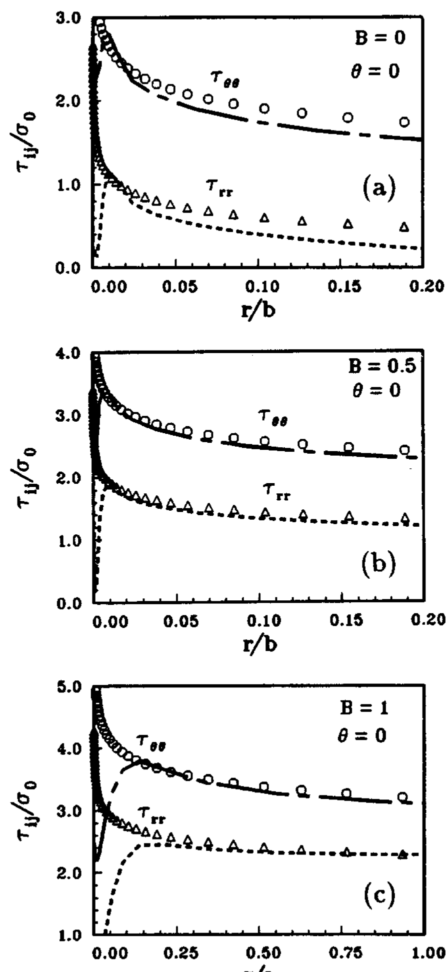

FIG. 12. Stresses in center-cracked panel, $a/W = 0.1$, at load levels shown in Fig. 7 for $B = 0$, 0.5, and 1.0. Two-term expansion shown by open circles. $Q = -1.2$, -0.4, and 0.2, $\hat{\tau}_{rr} = 1.3$, 1.3, and 1.0, respectively.

scale yielding to fully yielded conditions. At the latter three loads levels, the stresses have settled to nearly identical stress distributions. The second-order stresses at the fully yielded state for $B = 0.5$ are plotted in Fig. 10(b) and (d).

Figure 11 show the stress distributions produced by the high-biaxiality case $B = 1$. Good agreement between the full-field solution and the HRR field over the entire load range can be seen. Q reaches a steady-state value almost immediately.

The distributions for all biaxial load states can be identified with members of the Q-family of fields shown in Figs 3 and 4. $B = 0$ corresponds to a low-constraint state $Q < 0$, $B = 0.5$ corresponds to an intermediate state, and $B = 1$ corresponds to a high-constraint state $Q \geqslant 0$. We have carried out calculations for $B > 1$ but have not been able to generate near-tip stress levels higher than those produced by $B = 1$.

A comparison of the stresses at the fully yielded state, $a\sigma_0/J = 8$, 12, and 10, for $B = 0$, 0.5, and 1 with the two-term expansion (2.9) is provided in Fig. 12. In Fig. 12(a) and (b) distance is normalized by the ligament length b, and in Fig. 12(c) by the crack length a as these are the relevant lengths (see Fig. 7). The Q values of -1.2, -0.4, and 0.2, respectively, were chosen to give the best fit with the full-field hoop stress over 5% of the plastic zone. Indeed, the good agreement over a significant fraction of the plastic zone confirms the existence of a J–Q annulus.

5.2. *Deep crack tension geometry*, a/W = 0.7

The plastic zones in the right half of the panel at fully yielded conditions, for $B = 0$, 1, and 2 are shown in Fig. 13. For $B \geqslant 2$, the plastic zone does not spread across the ligament. Instead it evolves backwards to the mid-section and finally links up to form a plastic annulus that completely surrounds the crack. We attempted to generate even higher-triaxiality near-tip fields using $B > 2$. However, we found that the maximum stress levels that develop for load states $B > 2$ did not exceed the level for $B = 2$.

The trends of the full-field solutions for deeply cracked geometry are similar to those for the shallow-crack geometry. To illustrate this point, the second-order stress terms ahead of the crack $Q\hat{\tau}_{\theta\theta}$ and $Q\hat{\tau}_{rr}$ are plotted in Fig. 14 for the three biaxiality load states. The similarity with the distributions in Figs 8(b) and (d), 10(b), and 11(b)

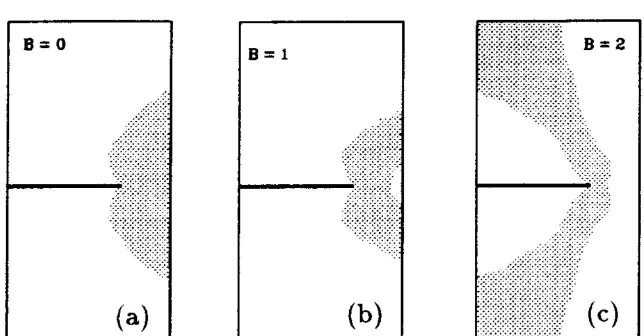

FIG. 13. Plastic zones in right half of center-cracked panel, $a/W = 0.7$, for $B = 0$, 1, and 2 at fully yielded conditions. Remote stress levels are $\sigma_{yy}^{\infty}/\sigma_0 = 0.5$, 0.5, and 0.6, respectively.

is seen. Though not shown we observe weak angular dependence of the second-order terms in the sector $|\theta| < \pi/2$. Figure 15 shows the full-field solution for $B = 0$, 1, and 2 at $b\sigma_0/J = 60$, 35, and 35, respectively. The two-term expansion shown by the open circles accurately represents the full-field solution. Here the Q values are -0.9, -0.45, and -0.15, respectively.

5.3. *Shallow-crack three-point bend geometry*, a/W = 0.1

The geometry of the three-point bend bar is shown in Fig. 1(c). The plastic zones corresponding to two states of contained yielding, $a/(J/\sigma_0) = 30$ and 20, and the fully

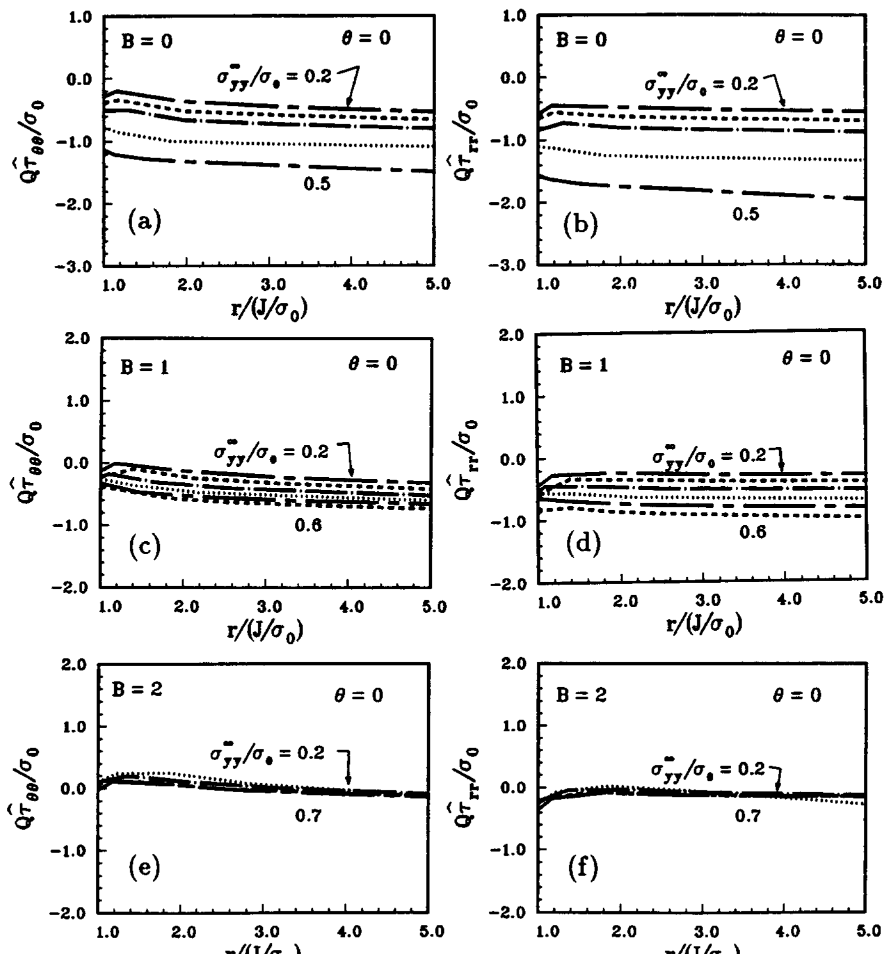

FIG. 14. Second-order terms in center-cracked panel, $a/W = 0.7$, for load states from small-scale to fully yielded conditions. (a) and (b) $\sigma_{yy}^{\infty}/\sigma_0 = 0.2$, 0.25, 0.3, 0.4, and 0.5, corresponding to $b\sigma_0/J = 400$, 250, 170, 65, and 10. (c) and (d) $\sigma_{yy}^{\infty}/\sigma_0 = 0.2$, 0.3, 0.4, 0.5, and 0.6, corresponding to $b\sigma_0/J = 400$, 180, 90, 50, 30, and 20. (e) and (f) $\sigma_{yy}^{\infty}/\sigma_0 = 0.4$, 0.5, 0.6, and 0.7, corresponding to $b\sigma_0/J = 100$, 60, 35, and 12.5.

yielded state, $a/(J/\sigma_0) = 5$ are shown in Fig.16. Figure 17(a) and (b) show the behavior of the stresses ahead of the crack for the full range of states from small-scale yielding to fully yielded conditions corresponding to $a/(J/\sigma_0) = 850$, 200, 110, 50, 15, and 5; the HRR distribution is indicated by the solid circles. The second-order terms are shown in Fig. 17(b) and (d). Figure 18 shows the behavior of these quantities along $\theta = \pi/4$. Note that $\hat{\tau}_{r\theta}$ is practically zero at all load levels. Observe that $Q\hat{\tau}_{\theta\theta}$ for $a/(J/\sigma_0) = 5$ decreases with distance at both angles [see Figs 17(b) and 18(b)]. This behavior arises because the crack opening is now a sizable fraction of the crack length. Under these conditions, the relevance of fracture mechanics is questionable.

Figure 19 provides a comparison of the two-term expansion and the full-field

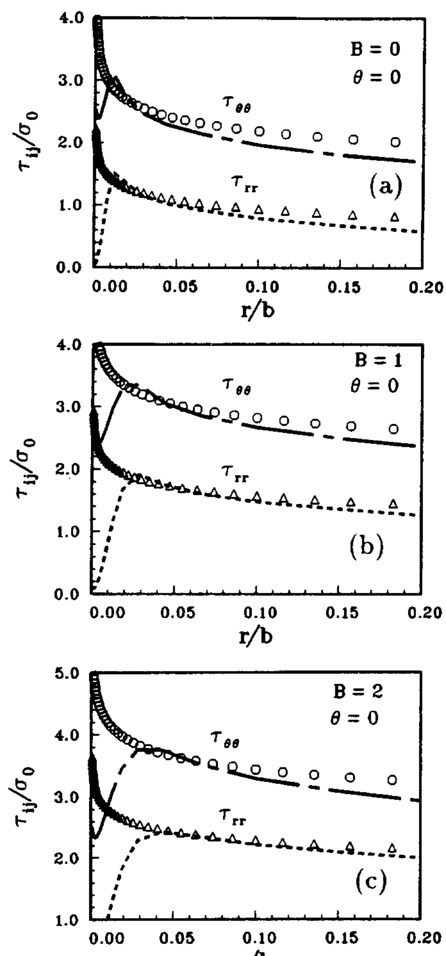

FIG. 15. Stresses in center-cracked panel, $a/W = 0.7$, at fully yielded state for $B = 0$, 1, and 2 for the stress levels in Fig. 13. Two-term expansion shown by open circles. $Q = -0.9$, -0.45, and 0.15, $\hat{\tau}_{rr} = 1.3$, 1.3, and 1.0, respectively.

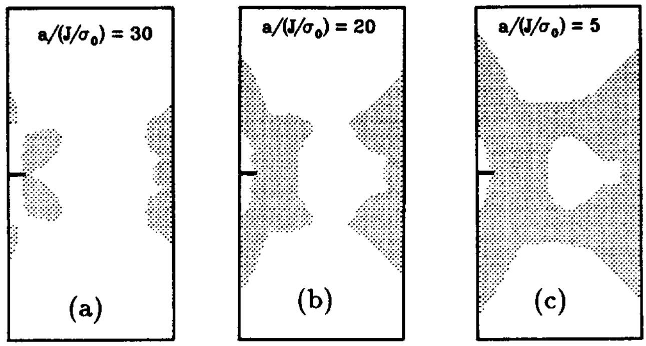

FIG. 16. Plastic zones in three-point bend bar, $a/W = 0.1$, for contained yielding, large-scale yielding, and fully yielded conditions.

solution for three load levels. Here the Q values are -0.75, -0.75, and -0.8, respectively. The fields are in good agreement over a sizable fraction of a, the relevant dimension of the shallow-crack geometry. However, the excessive blunting in Fig. 19(c) is noted. The agreement in this case may be fortuitous.

We have also analyzed this geometry with $a/W = 0.2$, 0.3, and 0.5. The fields that evolve in the $a/W = 0.2$ geometry are rather similar to those for the $a/W = 0.1$ shown in Figs 17 and 18. Our results show that the $a/W = 0.5$ geometry behaves exactly like

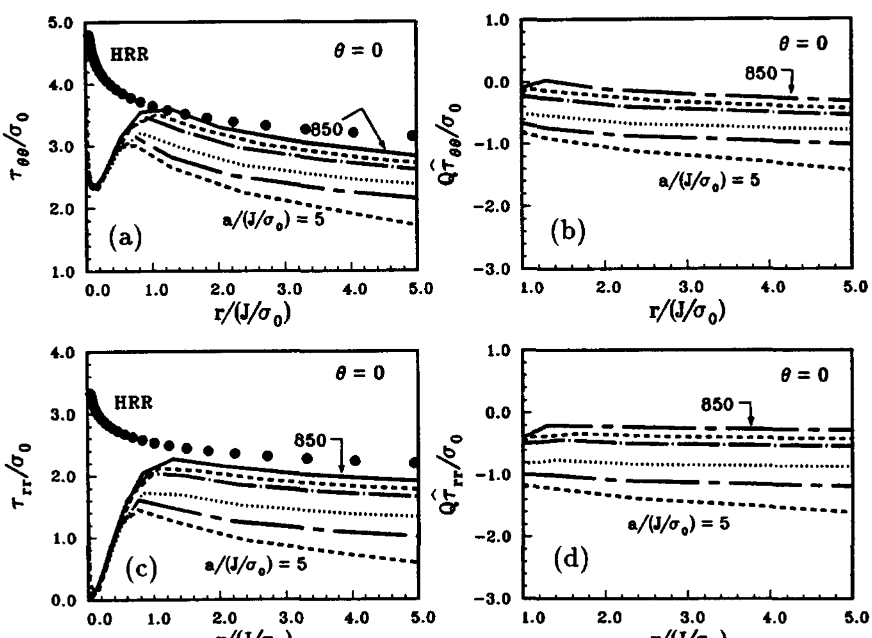

FIG. 17. Stresses in three-point bend bar, $a/W = 0.1$, from small-scale to fully yielded conditions, $a/(J/\sigma_0) = 850$, 200, 100, 50, 15, and 5. (a) and (c) Stresses at $\theta = 0$. HRR field is indicated by solid circles. (b) and (d) Second-order terms at $\theta = 0$.

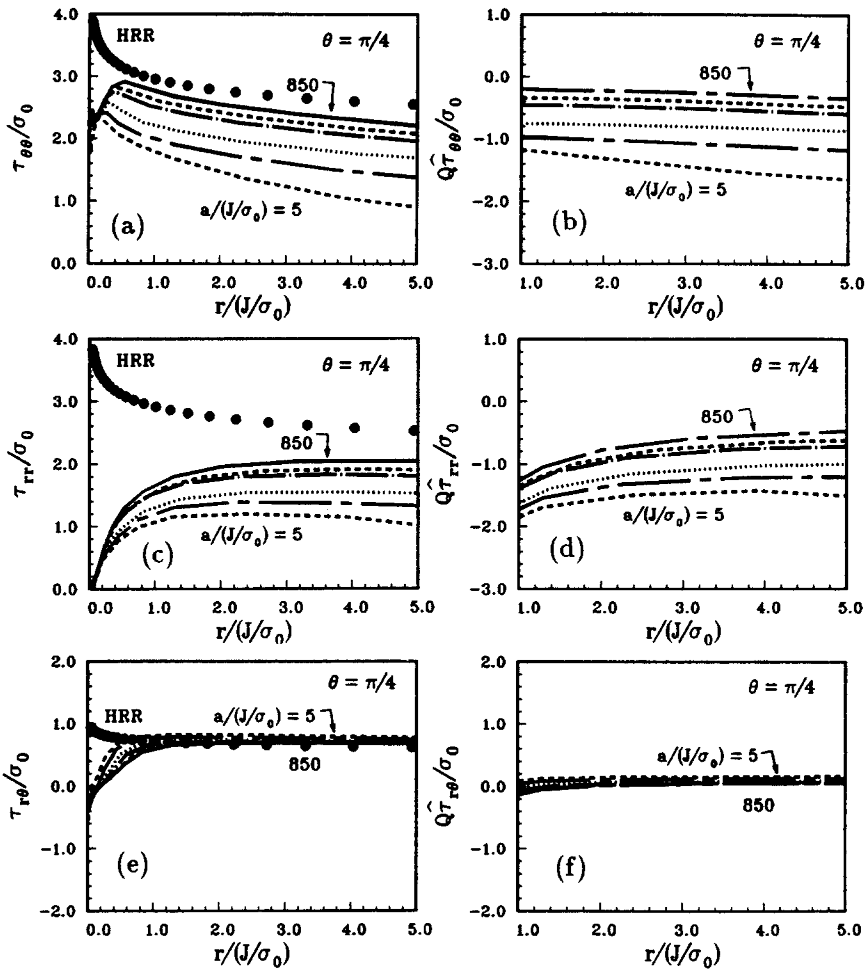

FIG. 18. Stresses in three-point bend bar, $a/W = 0.1$, at the load levels given in Fig. 17. (a), (c) and (e) Stresses at $\theta = \pi/4$. HRR field is indicated by solid circles. (b), (d) and (f) Second-order terms at $\theta = \pi/4$.

that of a deeply cracked geometry as reported by McMEEKING and PARKS (1979), SHIH and GERMAN (1981), and NEEDLEMAN and TVERGAARD (1983). In each case the fields that develop can be identified with members of the Q-family provided that the characteristic crack dimension is much larger. Our results are consistent with the conclusions reached by AL-ANI and HANCOCK (1991), who have conducted an extensive investigation of the shallow-crack geometry.

6. CONCLUDING REMARKS

We have demonstrated that the plastic near-tip fields are characterized by two parameters, J and Q. The stress distribution and the maximum stress depend on Q

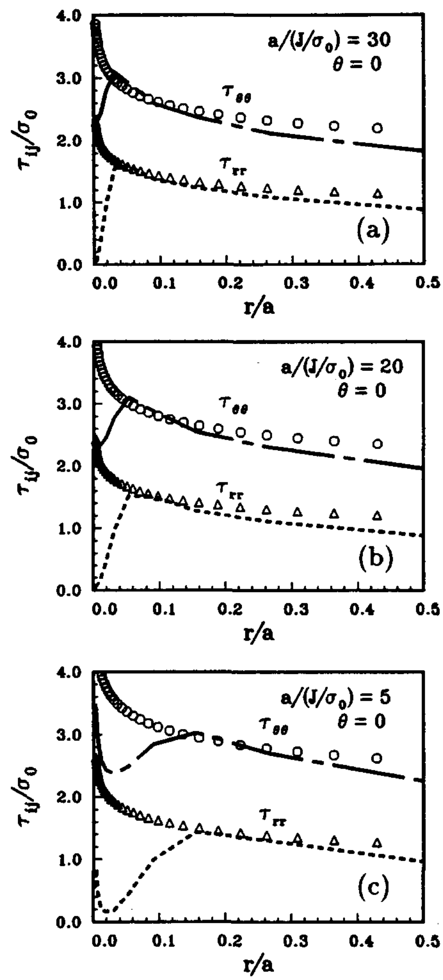

FIG. 19. Stresses in three-point bend bar, $a/W = 0.1$, at $a/(J/\sigma_0) = 30$, 20, and 5. Two-term expansion shown by open circles. $Q = -0.75$, -0.75, and -0.8, $\hat{\tau}_{rr} = 1.2$, 1.2, and 1.3, respectively.

alone while J sets the size scale over which large stresses and large strains develop. Furthermore, we have observed that this Q-family of fields continues to exist in different crack geometries at large-scale yielding when the relevant crack dimension is much larger than J/σ_0. The Q value depends on crack geometry and the extent of plastic yielding. For certain crack geometries Q reaches a steady-state value when fully plastic conditions are approached. The range $-2.0 < Q < 0.2$ covers every stress distribution that has been generated in this investigation.

The Q-family of solutions provides a framework for quantifying the evolution of constraint from small-scale yielding to fully yielded conditions, and the limiting (steady-state) constraint when it exists. Thus Q can be used to rank crack geometries according to constraint. More importantly, fracture toughness and possibly fracture resistance curve can be phrased as a function of Q, i.e. $J_C(Q)$ and $J_R(\Delta a, Q)$. For example, the toughness values determined from low-constraint specimens ($Q < 0$), e.g. shallow-crack geometries, and high-constraint specimens ($Q \geqslant 0$), e.g. deeply cracked bend bars, can be organized into a single toughness curve by the Q-parameter. Specifically, toughness values for $Q \geqslant 0$ can be determined using test specimens which meet the required size restrictions for J-dominance as discussed in ASTM Standards E 813-87 for J_{IC} testing.

ACKNOWLEDGEMENTS

This investigation is supported by the Office of Naval Research through ONR Grant "Computational and Experimental Investigation of Elastic–Plastic Fracture under Dynamic Conditions". The computations were performed at the Computational Mechanics Facility of Brown University. The acquisition of the computers in the Facility was made possible by grants from the U.S. National Science Foundation (Grant DMR-8714665), and the Office of Naval Research (Grant N00014-88-K-0119), and matching funds from Brown University.

REFERENCES

AL-ANI, A. M. and HANCOCK, J. W.	1991	*J. Mech. Phys. Solids* **39**, 23.
BETEGÓN, C. and HANCOCK, J. W.	1990	To appear in *J. appl. Mech.*
BILBY, B. A., CARDEW, G. E., GOLDTHORPE, M.R. and HOWARD, I. C.	1986	*Size Effects in Fracture*, p. 37. Institution of Mechanical Engineers, London.
CHEN, X. Y. and DRUGAN, W. J.	1990	Submitted for publication.
DRUGAN, W. J. and CHEN, X. Y.	1989	*J. Mech. Phys. Solids* **37**, 1.
DU, Z.-Z. and HANCOCK, J. W.	1991	*J. Mech. Phys. Solids* **39**, 555.
ESHELBY, J. D.	1970	*Inelastic Behavior of Solids* (edited by M. F. KANNINEN *et al.*), p. 77. McGraw-Hill, New York.
HUTCHINSON, J. W.	1968	*J. Mech. Phys. Solids* **16**, 13.
HUTCHINSON, J. W.	1983	*J. appl. Mech.* **50**, 1042.
LARSSON, S. G. and CARLSSON, A. J.	1973	*J. Mech. Phys. Solids* **21**, 263.
LI, F. Z., SHIH, C. F. NEEDLEMAN, A.	1985	*Engng Fracture Mech.* **21**, 405.
LI, Y. C. and WANG, T. C.	1986	*Scientia sin.* (*Ser. A*) **29**, 941.
MCMEEKING, R. M.	1977	*J. Mech. Phys. Solids* **25**, 357.
MCMEEKING, R. M. and PARKS, D. M.	1979	*Elastic–Plastic Fracture Mechanics*, ASTM-STP-668, p. 175. American Society for Testing and Materials, Philadelphia, PA.
MORAN, B. and SHIH, C. F.	1987	*Engng Fracture Mech.* **27**, 615.
MORAN, B., ORTIZ, M. and SHIH, C. F.	1990	*Int. J. Numerical Meth. Engng* **29**, 483.
NEEDLEMAN, A. and TVERGAARD, V.	1983	*Elastic–Plastic Fracture: Second Symposium Volume I—Inelastic Crack Analysis*, ASTM-STP-803, p. 80. American Society for Testing and Materials, Philadelphia, PA.
PARKS, D. M.	1977	*Computational Meth. appl. Mech. Engng* **12**, 353.

PARKS, D. M. 1989 Presented at the European Group Fracture Symposium, Freiberg, Germany, 1990. Submitted for publication.
RICE, J. R. 1968 *J. appl. Mech.* **35,** 379.
RICE, J. R. 1974 *J. Mech. Phys. Solids* **22,** 17.
RICE, J. R. and JOHNSON, M. A. 1970 *Inelastic Behavior of Solids* (edited by M. F. KANNINEN *et al.*), p. 641. McGraw-Hill, New York.
RICE, J. R. and ROSENGREN, G. F. 1968 *J. Mech. Phys. Solids* **16,** 1.
SHARMA, S. M. and ARAVAS, N. 1991 *J. Mech. Phys. Solids* **39,** 1043.
SHIH, C. F. 1981 *J. Mech. Phys. Solids* **29,** 305.
SHIH, C. F. 1985 *Int. J. Fracture* **29,** 73.
SHIH, C. F. and GERMAN, M. D. 1981 *Int. J. Fracture* **17,** 27.
SYMINGTON, M., SHIH, C. F. and ORTIZ, M. 1988 Brown University Report, MRG/DMR-8714665/1.
WILLIAMS, M. L. 1957 *J. appl. Mech.* **24,** 111.